



## An implicit joint-continuum model for the hydro-mechanical analysis of fractured rock masses

Hosung Shin<sup>a,\*</sup>, J. Carlos Santamarina<sup>b</sup>

<sup>a</sup> Dept. of Civil & Environmental Eng., University of Ulsan, Saudi Arabia

<sup>b</sup> Earth Science and Engineering, KAUST, Saudi Arabia



### ARTICLE INFO

#### Keywords:

Fractured rock mass  
Hydro-mechanical coupling  
FEM  
Hydraulic stimulation  
Affiliations

### ABSTRACT

Fractures control the hydro-mechanical behavior of rock masses. Explicit numerical analyses require detailed information on fracture properties, spacing, and orientation. This paper advances an implicit joint-continuum model for the coupled hydro-mechanical analysis of regularly spaced-persistent fractured rock masses. The stiffness tensor combines the compliance of each fracture set and the intact rock; similarly, the permeability tensor adds the fluid transport through fractures and the matrix. The fully coupled hydro-mechanical analysis incorporates the rock mass stiffness and permeability tensors, and satisfies force equilibrium and macroscopic fluid mass balance. We implement the implicit joint-continuum model within a finite element framework and verify the numerical simulator against closed-form solutions for simple boundary conditions. The application of the code to the hydraulic stimulation of a fractured rock mass shows the effect of stress anisotropy and fracture orientation on the development of open-mode discontinuities (i.e., hydraulic fracture) and hydro-shearing. The implicit joint-continuum model can be readily extended to more complex coupled processes, including thermal and chemical phenomena.

### 1. Introduction

A rock mass consists of intact rock blocks separated by fractures, fissures, faults, and bedding planes. Discontinuities vary over a wide range of length scales and convey anisotropic and heterogeneous engineering properties to the rock mass.<sup>1,2</sup>

Important fracture characteristics are orientation, surface roughness, persistence, degree of interconnectivity, separation and aperture.<sup>3</sup> Fractures have a much higher compliance and permeability than the surrounding intact rock, are dominant conduits for fluid transport, and favor localized mechanical deformation.

Shear-induced fracture dilation and contraction can cause dramatic changes in the hydraulic transmissivity tensor and the fluid pressure field in the rock mass. Associated changes in the effective stress will cause additional fracture deformation.<sup>4</sup> Clearly, the coupled hydro-mechanical behavior of a fractured rock mass is of great interest to infrastructure engineering, radioactive waste disposal, the recovery of geothermal energy, CO<sub>2</sub> geological storage, oil and gas recovery and tectonic faulting.<sup>5,6</sup>

Numerical models of fractured rock masses fall under discontinuous or continuous-media models. Discontinuous-media models such as the Distinct Element Method and the Discontinuous Deformation Analysis

use discrete block systems to form the rock mass.<sup>7,8</sup> These simulations are computationally demanding for large-scale and long-term predictions, and are limited by the available fracture distribution data.<sup>9</sup> Hydro-mechanical coupling in discontinuous-media models typically involves the separate solution of fluid flow and deformation equations followed by ambiguous numerical steps to link the two.<sup>10</sup> Furthermore, these uncoupled-recoupled numerical procedures hinder the implementation of additional coupled processes such as thermal effects.

By contrast, continuous-media models involve fully coupled governing equations at the element level. Consequently, they are most valuable to model the coupled hydro-mechanical behavior of rock masses for complex engineering problems. Continuum methods can be categorized in terms of the length scale of problem  $L$  relative to the fracture spacing  $s$ ,  $L/s$ . Classical equivalent-continuum models can represent highly fractured rock masses ( $L/s \gg 1$ ) but disregard preferential fracture orientations.<sup>11</sup> On the other extreme, explicit joint-continuum models introduce interfacial elements to represent each discontinuity.<sup>12,13</sup> These are simple to implement into finite element simulators, but are only practical for the analyses of a small number of fractures within the volume of interest ( $L/s \sim 1$ ). For intermediate cases ( $L/s > 1$ , but limited), implicit joint-continuum models incorporate fracture sets with a regular geometric configuration into the rock mass;

\* Corresponding author.

E-mail address: [shingeo@ulsan.ac.kr](mailto:shingeo@ulsan.ac.kr) (H. Shin).

the resulting equivalent continuum combines the fracture and the matrix deformation and flow properties. The meaning of an “implicit” model is to take into account the discontinuous effect of regularly spaced-planar-persistent fracture sets in an implicit way on continuum-based modeling.

Previous implicit-joint models captured the effects of fractures in the elastic compliance tensor for the fractured rock mass with various degree of success with orthogonal fracture sets<sup>14–16</sup> and randomly oriented fracture sets.<sup>17–19</sup> In fact, there is still no definitive derivation of the elastic compliance tensor for a rock mass with a general fracture orientation. Furthermore, there is no consistent continuum representation of the elasto-plastic response of a fractured rock mass where the preferred displacement direction is kinematically defined by the fracture planes.<sup>20</sup>

This manuscript documents the development and validation of a three-dimensional hydro-mechanically coupled implicit joint-continuum model for a rock mass with one or several persistent fracture sets of arbitrary orientation and spacing. Mathematical models, code verification and practical examples follow.

## 2. Formulation of the proposed model

The proposed formulation assumes that fracture sets are made of persistent, quasi-planar parallel fractures with regular spacing (Fig. 1 – XYZ global coordinate system). The fracture strike  $\theta$  is the angle measured clockwise between the North direction (+Y) and the intersection line formed by the joint plane and the XY surface. The dip angle  $\beta$  is the steepest angle formed by the fracture plane and the XY surface. Therefore, the vectors that define strike, dip and the vector normal to the fracture plane are functions of  $\theta$  and  $\beta$  in the local xyz coordinate system:

$$\underline{n}^y = (\sin \theta, \cos \theta, 0)\text{strike direction} \quad (1)$$

The fracture spacing  $s$  is the normal distance between two adjacent fracture planes in a set. Therefore, the fracture spacing  $s_i$  in the global XYZ axes is  $(s_i \underline{e}^i) \cdot \underline{n}^z = s$  where vectors  $\underline{e}^i$  form the orthonormal bases in the XYZ space.

Lower index in notations is for global or local coordinate system, and upper index for the vector sequence to define the fracture plane throughout the whole paper. In coordinate system, small letter of the symbol is for local coordinate on the fracture plane (e.g.  $u_p$ ), and capital letter for global coordinate systems (e.g.  $U_i$ ).

### 2.1. Mechanical model

Stress changes deform intact rock blocks and cause fracture displacements. The overall mechanical behavior of the fractured rock mass

combines the intact rock and fracture sets in series and satisfies stress continuity across the fracture plane.

**Compliance tensor for the fractured rock mass.** The applied stress  $\underline{\sigma}$  and the fracture orientation define the stress components on the fracture plane  $S$ ; for example, the stress component on the fracture plane caused by the applied stresses in the Z-direction follows from equilibrium,

$$S_q = n_z^z \cdot \sigma_{zj} \cdot n_i^q = \frac{n_z^z}{2} (n_k^q \cdot \delta_{3l} + n_l^q \cdot \delta_{3k}) \cdot \sigma_{kl} \quad (2)$$

where  $\underline{\sigma}$  is a 2nd order stress tensor  $\sigma_{ij}$ ,  $\delta_{ij}$  is Kronecker delta, and  $\underline{a} \cdot \underline{b}$  is the inner product of two vectors  $\sum_{i=1}^3 a_i b_i = \underline{a} \cdot \underline{b}$ . Super-indices and sub-indices range over the set {1,2,3}.

The elastoplastic fracture stiffness matrix  $d_{pq}^J$  relates the stress  $S_q$  on a fracture plane to displacements  $S_p = d_{pq}^J \cdot u_q$ ; conversely,  $u_p = c_{pq}^J \cdot S_q$  where the joint stiffness matrix  $d_{pq}^J$  is the inverse of the joint compliance matrix  $c_{pq}^J = d_{pq}^J{}^{-1}$ . The stress transformation in Equation (2) combines with the fracture compliance matrix to provide the relationship between the fracture displacement  $u_p$  and the acting stresses  $\underline{\sigma}$  in the Z direction,

$$u_p = c_{pq}^J \cdot \frac{n_z^z}{2} (n_k^q \cdot \delta_{3l} + n_l^q \cdot \delta_{3k}) \cdot \sigma_{kl} \quad (3)$$

The displacement along the fracture  $u_p$  leads to the strain tensor  $\epsilon_{ij}^J$  in the XYZ global coordinate system through two sequential steps: (1) compute the global displacement  $U_i$  in the Z direction for a rock mass of unit length from the local joint displacement,  $U_i = u_k \cdot n_i^k / s_z$ ; and (2) compute the strains in the Z direction that result from these global displacements  $\epsilon_{ZZ}^J = U_Z$ ,  $\gamma_{ZX}^J = U_X$  and  $\gamma_{ZY}^J = U_Y$ . We assume a symmetric strain tensor analogous to continuum mechanics,<sup>21</sup> and assemble the strain tensor  $\epsilon_{ij}^J$  for the given fracture displacement and fracture spacing

$$\epsilon_{ij}^J = \frac{n_z^z}{2 \cdot s} (n_i^p \delta_{3j} + n_j^p \delta_{3i}) \cdot u_p \quad (4)$$

Equations (3) and (4) give a mechanical relationship between the applied stress tensor  $\underline{\sigma}$  and the induced joint strain tensor  $\epsilon_{ij}^J$  in the Z direction. The same procedure computes the compliance tensors in the X and Y directions. The compliance tensor  $C^J$  of a fracture set sums the compliances in each global direction. Finally, the stress-strain relationship for a single fracture set is:

$$\epsilon_{ij}^J = C_{ijkl}^J \sigma_{kl} = \sum_r \frac{n_r^z}{4 \cdot s} (n_i^p \delta_{rj} + n_j^p \delta_{ri}) \cdot c_{pq}^J \cdot n_r^z \cdot (n_k^q \cdot \delta_{rl} + n_l^q \cdot \delta_{rk}) \cdot \sigma_{kl} \quad (5)$$

where the 4th order compliance tensor  $C^J$  represents the deformation effect of a fracture set on the rock mass.

The compliance tensor  $C^m$  for the rock mass with multiple fracture

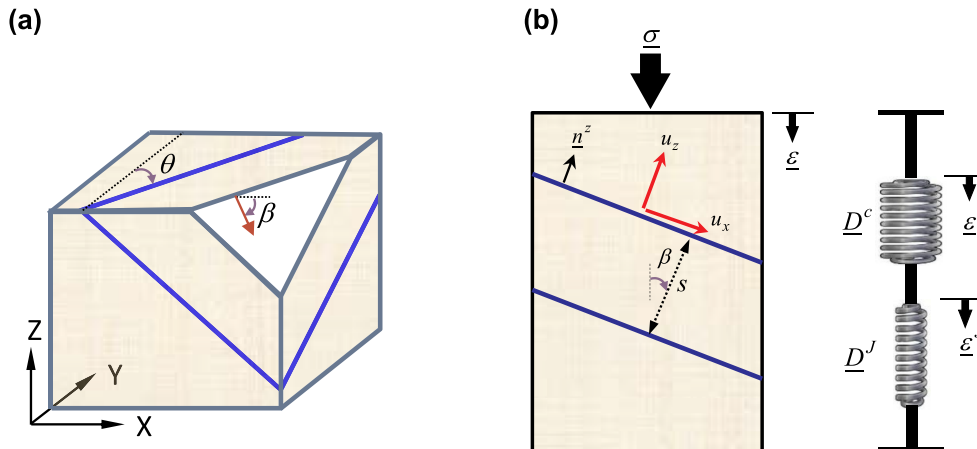


Figure 1. Fractured rock mass – Definitions. (a) Coordinate system and fracture orientation. (b) Schematic model for mechanical analysis

sets adds the compliance tensors for each fracture set  $C^J$  and that of the intact rock

$$\underline{\varepsilon} = \underline{\varepsilon}^c + \sum C^J = (C^c + \sum C^J) \underline{\sigma} = C^m \underline{\sigma} \quad (6)$$

The numerical algorithm involves two steps. First, it updates the stresses for the intact rock and each fracture set. Then, it distributes the strain increments  $\underline{\varepsilon}$  from the previous trial step into the intact rock  $\underline{\varepsilon}^c$  and each fracture set  $\underline{\varepsilon}^J$ . The stress continuity between the intact rock and fractures determines the strain increment of the intact rock and each joint set from the total strain increment,

$$\begin{aligned} d\underline{\varepsilon}^c &= C^c: D^m: d\underline{\varepsilon} \\ d\underline{\varepsilon}^J &= C^J: D^m: d\underline{\varepsilon} \end{aligned} \quad (7)$$

where  $\underline{a}: \underline{b}$  is the 2nd order inner product in tensor calculations,  $a_{ij}b_{ij}$ .

The stiffness tensor  $D^m = C^{m-1}$  of the jointed rock mass relates the strain increment to the stress increment  $d\underline{\sigma} = D^m d\underline{\varepsilon}$  and is required to build the global stiffness matrix in the finite element simulator.

**Constitutive models.** We adopt an elasto-plastic behavior for the intact rock. The Mohr-Coulomb failure criterion is defined by the friction angle  $\phi_p$  and cohesion  $c$  of the intact rock:  $\tau_f = c + \sigma_n \tan(\phi_p)$ . The numerical implementation of this model computes the stiffness tensor  $D^c$  from the compliance tensor  $C^c$  (Equation (6)), and updates stresses components.<sup>22</sup>

The non-linear constitutive model for fractures captures normal stiffness, shear stiffness and strength (Examples of complex fracture response<sup>16,23–25</sup>). Detailed descriptions follow:

- (i) Normal stiffness  $K_n$ : The tangential normal stiffness describes the closing or opening response of the fracture to the imposed normal stress. We select a hyperbolic stress-aperture relationship.<sup>26</sup>

$$K_n = K_{no} \left( 1 - \frac{\sigma_n}{\sigma_n + e_{\min} K_{no}} \right)^{-2} \quad (8)$$

where  $K_{no}$  is the normal stiffness at zero normal stress, and  $e_{\min}$  is the terminal fracture aperture at high normal stress.

- (ii) Shear stiffness  $K_s$ : The fracture shear stiffness is lower than the normal stiffness  $K_n$  but tracks its evolution; therefore, we relate  $K_s$  to  $K_n$  by a stiffness ratio  $k_r = K_s/K_n$ . Empirical evidence shows that the stiffness ratio depends on the degree of weathering, normal stress, and rock type.<sup>26–29</sup>
- (iii) Strength: The fracture shear follows the Coulomb failure criterion and combines friction  $\phi_b$  and dilation against asperities. Then, the peak strength  $\tau_f$  is a function of the effective normal stress  $\sigma_n$ :

$$\tau_f = \sigma_n \tan(\phi_b + \alpha) \quad (9)$$

The asperity angle  $\alpha$  decreases during shear as an exponential function of the shear plastic work  $W_p, \alpha = \alpha_0 \exp(-\lambda_\alpha \cdot W_p)$ <sup>30,31</sup>

**Numerical formulation for the fracture model.** The elastoplastic stiffness matrix  $S_i = d_{ij}^J \cdot u_j$  describes the fracture elastic response and shear strength. The displacement increment for each fracture set is proportional to its compliance tensor (Equation (7)). The consistent tangent formulation computes the stiffness matrix and updated stresses. This formulation ensures a quadratic rate of asymptotic convergence.<sup>32</sup>

Given a failure function  $f = \sigma_s - \sigma_n \tan(\phi_b + \alpha)$  and a plastic potential function  $g = \sigma_s - \sigma_n \tan(\alpha)$ , the updated stress components  $\underline{S}^{(n+1)}$  and the stiffness matrix  $\underline{d}^J$  are obtained as a function of the plastic multiplier  $\Delta\lambda$ .

$$\Delta\lambda = \frac{|\underline{\tau}^T| - (\underline{S}^T: \underline{\delta}) \tan(\phi_b + \alpha)}{K_s + K_n \tan(\phi_b + \alpha) \tan \alpha} \quad (10)$$

where the shear stress  $\tau$  in the fracture results from the stresses acting on the fracture plane  $\underline{\tau} = \underline{S} - S_z \underline{\delta}$  ( $\underline{S} = [S_x, S_y, S_z]$ ), therefore the shear stress magnitude on the fracture plane is  $\sigma_s = |\underline{\tau}|$  and its direction

is  $\underline{n} = \underline{\tau}/\sigma_s$ . Then,

$$\underline{S}^{(n+1)} = |\underline{S}^T| - \Delta\lambda (K_s \underline{n} - K_n \tan \alpha \underline{\delta}) \quad (11)$$

$$\begin{aligned} \underline{d}^J &= K_n \underline{\delta} \otimes \left( \underline{\delta} + \tan \alpha \frac{\partial \Delta\lambda}{\partial \underline{u}} \right) + \alpha_s^{(n+1)} \frac{K_s}{|\underline{S}^T|} (\underline{1} - \underline{\delta} \otimes \underline{\delta} - \underline{n} \otimes \underline{n}) \\ &+ K_s \underline{n} \otimes \left( \underline{n} - \frac{\partial \Delta\lambda}{\partial \underline{u}} \right) \end{aligned} \quad (12)$$

When the fracture elastic stiffness matrix is  $\underline{d}^{Je} = K_s (\underline{1} - \underline{\delta} \otimes \underline{\delta}) + K_n \underline{\delta} \otimes \underline{\delta}$ , the trial stress component on the fracture is  $\underline{S}^T = \underline{S}^{(n)} + \underline{d}^{Je} \cdot \Delta \underline{u}$ , and the Dyadic product is  $\underline{a} \otimes \underline{b} = a_i b_j$ . The derivative of the plastic multiplier with respect to the fracture displacement is  $\frac{\partial \Delta\lambda}{\partial \underline{u}} = (K_s \underline{n} - K_n \tan(\phi_b + \alpha) \underline{\delta}) / (K_s + K_n \tan(\phi_b + \alpha) \tan(\alpha))$ . The plastic energy dissipation due to frictional sliding is  $W_p = \int \sigma_s \cdot d\underline{u}_s = \int \sigma_s \cdot d\underline{\lambda}$ .

The displacement increment  $\Delta \underline{u}$  induced by stress changes in the fractured rock determines the updated stress components  $\underline{S}^{(n+1)}$  on the fracture plane. The determinant of the stiffness matrix tends to zero at the peak strength for the elasto-perfect plastic model. We use the Moore-Penrose inverse to maintain numerical stability and to compute the stiffness tensor of the fractured rock mass from the compliance tensor in Equation (6).<sup>33</sup>

## 2.2. Hydraulic model

Fluid transport takes place through the intact rock and fractures. Fractures dominate the flow behavior and determine the “geoplumbing” of the rock mass in most cases.

**Intact Rock.** The fluid flow in the intact rock is darcian  $v_i = k_{ij}^c \cdot (-\partial h / \partial X_j)$  and a function of the intact rock permeability  $k_{ij}^c$ , where the gradient in total head  $\partial h / \partial X_j$  represents changes in both elevation and fluid pressure.

**Fractures.** Fluid flow along fractures occurs in a quasi-two-dimensional plane, controlled by the relative distribution of apertures along the fracture plane.<sup>34–36</sup> Laboratory studies show that fracture transmissivity varies with surface roughness, applied normal stress, aperture dilation during shear displacement, and gouge formation from asperity degradation.<sup>37–44</sup> The dilation of critically stressed fractures renders them most permeable.<sup>45,46</sup>

A cubic law  $T_o = \gamma \cdot e^3 / (12\mu)$  relates the smooth fracture aperture  $e$  to the transmissivity  $T_o$  for an incompressible fluid of unit weight  $\gamma$  and viscosity  $\mu$ . The hydraulic aperture  $e_h$  of a natural fracture is smaller than its mechanical aperture  $e_m$ .<sup>37,39,47,48</sup> The hydraulic aperture  $e_h$  evolves with the mechanical aperture  $e_m$  during the fracture normal deformation and shear-induced gouge production,<sup>49</sup>

$$e_h = e_{ho} + f \Delta e_m \quad (13)$$

We assume that the change in mechanical aperture  $\Delta e_m$  equals the normal fracture displacement  $u_z$ . The proportionality factor  $f$  is a function of the plastic work  $f = f_0 \exp(-c_f W_p)$  in agreement with the mechanical model described above.<sup>30</sup>

The transmissivity tensor for a single fracture has two equal in-plane components and a zero out of plane component  $\underline{T}^j = T_0 (\underline{1} - \underline{\delta} \otimes \underline{\delta})$ . Then, the permeability tensor for a fracture set is  $\underline{k}^j = \underline{T}^j / s$  in the local coordinate system, since the number of joints per unit length is the reciprocal of the joint spacing  $s$ . The permeability tensor in the global coordinate system is  $\frac{1}{s} n_i^k n_j^l T_{kl}^j$ . Finally, the permeability tensor for multiple fracture sets in the global coordinate system is  $\sum k_{ij}^J = \sum \frac{1}{s} n_i^k n_j^l T_{kl}^j$ .

**Rock Mass.** We adopt Darcy's law to describe the fluid flow through the fractured rock mass in the global coordinate system  $v_i = k_{ij}^c \cdot (-\partial h / \partial X_j)$ . Flow through the fractured rock mass combines fluid transport through the intact rock and fracture sets.<sup>50</sup>

$$k_{ij} = k_{ij}^c + \sum k_{ij}^J \quad (14)$$

2.3. Extension

A broad range of fracture sizes hinders the use of continuum-based numerical methods for hydro-mechanical analyses.<sup>51</sup> Hierarchical fracture systems can be modeled as a combination of explicit large fractures embedded in an implicit joint-continuum that represents the rock matrix. This approach facilitates the implementation of combined statistical-deterministic multi-scale fracture systems for the study of fluid flow and hydro-mechanical coupling in complex rock masses.<sup>52–54</sup> The combined representation can model fracture persistence,<sup>55</sup> and simulate sudden shear dilations and flow paths that result from stress changes.<sup>42</sup>

3. Verification of the proposed model

We implemented the hydro-mechanical model described above in the multi-dimensional FEM simulator Geo-COUS (Geo-COUpled Simulator); this simulator has been designed and structured to investigate coupled phenomena in porous and fractured media subjected to multi-phase flow. The continuum elements for three-dimensional analyses involve 20 nodes for displacement and 8 nodes for fluid pressure.

We tested mechanical and fluid flow algorithms separately and for coupled cases, and compared results against analytical solutions obtained for simple boundary conditions. All tests involve a  $2m_x \times 2m_y \times 4m_z$  rock block that is discretized into 16 elements (1 m<sup>3</sup> each) and 141 nodes. The displacement boundary condition on the bottom plane is  $U_z = 0$  (Note: the center node is fixed  $U_x = U_y = U_z = 0$  to hold the block in position); all other five boundaries are stress-controlled. Table 1 summarizes the material parameters for the intact rock and fracture sets used in various tests. We adopt linear elastic and perfect plastic material properties to compare simulation results against analytical equations.

3.1. Deformation and strength with a single fracture set

Consider a rock mass with a fracture set at a dip angle  $\beta$  and spacing  $s$ . The analytical solution of the equivalent elastic compliance under vertical compression combines the compliance of the intact rock and the fracture set as in Equations (6).<sup>15,29</sup>

$$C^m = C^c + C^J = \frac{1}{E^c} + \frac{\cos^2 \beta}{K_n s} \left( \cos^2 \beta + \frac{\sin^2 \beta}{k_r} \right) \quad (15)$$

where  $E^c$  is the elastic modulus of the intact rock, and  $k_r = K_s/K_n$  is shear to normal stiffness ratio for the deformation along the fracture plane.

Fig. 2a shows the normalized elastic modulus  $E^m/E^c$  for a single fracture set as a function of the dip angle  $\beta$ , where the rock mass stiffness is the inverse of its compliance  $E^m = C^{m-1}$ . Numerical results

obtained with the implicit joint-continuum model match the analytical solution and accurately reproduce experimental results<sup>56,57</sup> – Note: some published analytical solutions appear incorrect under the same boundary conditions –<sup>14,16,17</sup> The shear displacement along fractures dominates the vertical deformation of the rock mass with a low stiffness ratio  $k_r$ . Therefore, the elastic modulus of the rock mass with a single fracture set at dip angle  $\beta$  can be lower than the elastic modulus when the fracture set is horizontal  $\beta = 0^\circ$ . The elastic moduli for different stiffness ratios  $k_r$  converge to the same values for dip angles  $\beta = 0^\circ$  and  $90^\circ$  (Fig. 2a).

A fractured rock mass fails through either the intact rock or along the fractures.<sup>2,3,58–60</sup> Therefore, the compressive strength  $\sigma_f$  of a rock mass with a single fracture set at dip angle  $\beta$  is limited by either the intact rock strength  $\sigma_f = \sigma_c \tan^2(45^\circ + \varphi/2) + 2c \tan(45^\circ + \varphi/2)$  or the shear resistance along the fracture plane  $\sigma_f = \alpha_c [1 + (1 + \tan^2 \beta) \cdot \tan \varphi' / (\tan \beta - \tan \varphi')]$ , in agreement with constitutive models in Section 2.1. Fig. 2b illustrates the variation in compressive strength as a function of the dip angle  $\beta$ . These numerical results match analytical predictions.

Fig. 2c and d explore the fractured rock mass deformation for three selected dip angles  $\beta = 10^\circ, 45^\circ$  and  $65^\circ$ . The vertical stress  $\sigma_z$  versus vertical displacement  $U_z$  plot shows that the vertical displacement for the elastic-to-plastic transition varies with the dip angle  $\beta$  (Fig. 2c). Fig. 2c shows the horizontal displacement  $U_x$  at the center of the top plane ( $X = 0$  m,  $Y = 0$  m,  $Z = 4$  m) versus its vertical displacement  $U_z$ ; the displacement ratio  $U_x/U_z$  becomes constant when either the intact rock fails or sliding shear develops along the fracture set (see Fig. 2d for  $\beta = 10^\circ$ ). The numerically computed displacement ratio  $U_x/U_z$  agrees with the analytical solution for the elastic deformation

$$\frac{U_x}{U_z} = \frac{2 \sin(2\beta) + \sin(4\beta)}{2 \sin^2(2\beta) + \frac{8}{k_r^{-1}-1} \left( 1 + \frac{K_n s}{E^c} - \sin^2 \beta \right)} \quad (16)$$

(Note: other authors reached different equations<sup>16,17</sup>). The displacement ratio  $U_x/U_z$  for slip-failure along a dip angle  $\beta$  with a dilation angle  $\alpha$  is  $U_x/U_z = 1/\tan(\beta - \alpha)$  in agreement with numerical results (Fig. 2d).

3.2. Deformation and strength with two fracture sets

We now consider a vertical compression test on the same block, but with two quasi-conjugate fracture sets such that  $\beta_2 - \beta_1 = \Delta\beta = 45^\circ$ . Fig. 3 shows a precise match between the analytical solution and numerical results computed using compliance addition (Equation (15)). Note that the elastic modulus of the rock mass does not have a simple  $\pi$ -periodicity, therefore transverse isotropy cannot reproduce the response of the implicit joint-continuum model in Fig. 3a. Shear sliding along the fracture sets limits the rock mass strength regardless of the fractures orientation (Note: parameters in Table 1a). The solid line in Fig. 3b shows the analytically computed strength envelope for the rock

Table 1  
Material properties in numerical simulation.

	Model	Properties
Figs. 2, 3, 4	Mechanical	Intact rock $E^c = 10^4$ MPa, $\nu = 0.3$ Plastic behavior $\sigma_c = 1$ MPa, $c = 0.5$ MPa, $\varphi = 30^\circ$ , $\delta = 30^\circ$
		Fracture set $K_n = 5 \times 10^3$ MPa/m, $k_r = 0.2/1.0$ , $e_m = 1$ cm, $s = 0.5$ m Plastic behavior $c = 0$ , $\varphi_b = 20^\circ$ , $\alpha = 20^\circ$
Figs. 5 and 6	Hydraulic	Intact rock $k_c = 10^{-12}$ m/s
		Fracture set Initial hydraulic aperture $e_{ho} = 2$ mm = constant
	Mechanical	Intact rock $E^c = 10^4$ MPa, $\nu = 0.3$ Fracture set $k_r = 0.2$ , $e_m = 2$ mm, $s = 0.2$ m Plastic behavior $c = 0$ , $\varphi_b = 30^\circ$ , $\lambda_\alpha = 50$ m/MN
	Hydraulic	Intact rock Normal stiffness: $K_{no} = 11.35$ MPa, $e_{min} = 2$ mm Fracture set $k_c = 10^{-12}$ m/s Initial hydraulic aperture $e_{ho} = 2$ mm

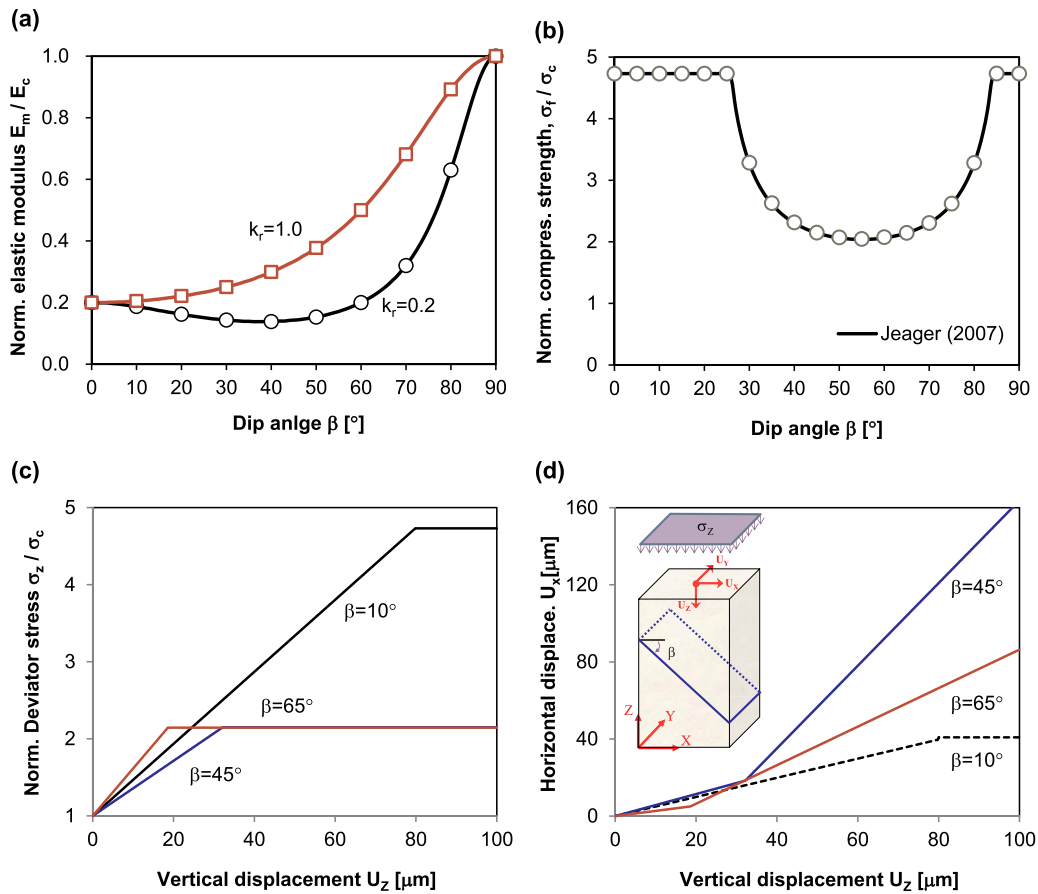


**Figure 2.** Mechanical model validation - Rock mass with a single fracture set subjected to vertical compression. (a) Rock mass stiffness normalized by the intact rock stiffness vs. fracture orientation. (b) Rock mass strength normalized by the confining stress vs. fracture orientation. (c) Normalized stress vs. displacement at three dip angles. (d) Horizontal vs. vertical displacements at three dip angles. Lines: analytical solution; data-points: numerical results. Confining stress 1.0 MPa. Material parameters in Table 1a.

mass with two fracture sets at  $\Delta\beta = 45^\circ$ . The solution combines the Mohr-Coulomb failure criterion and the envelope superposition method.<sup>2</sup> The numerical model predicts the same strength and failure modes as the analytical solution. Results in Fig. 3 highlight the prevalent role of fractures on the rock mass stiffness and strength.

3.3. Permeability and hydro-mechanical coupling

Consider a fractured rock mass with a single joint set (strike  $\theta = 0^\circ$ , dip angle  $\beta$ , spacing  $s$ ). The permeability in the global Z direction is  $k_{ZZ}^J = \frac{\gamma e h^3}{(12\mu \cdot s) \sin^2 \beta}$  (derived from Equation (14)). The predicted  $\sin^2$ -trend adequately matches hydraulic conductivity measurements gathered using sandstone samples cored at various orientations with respect to

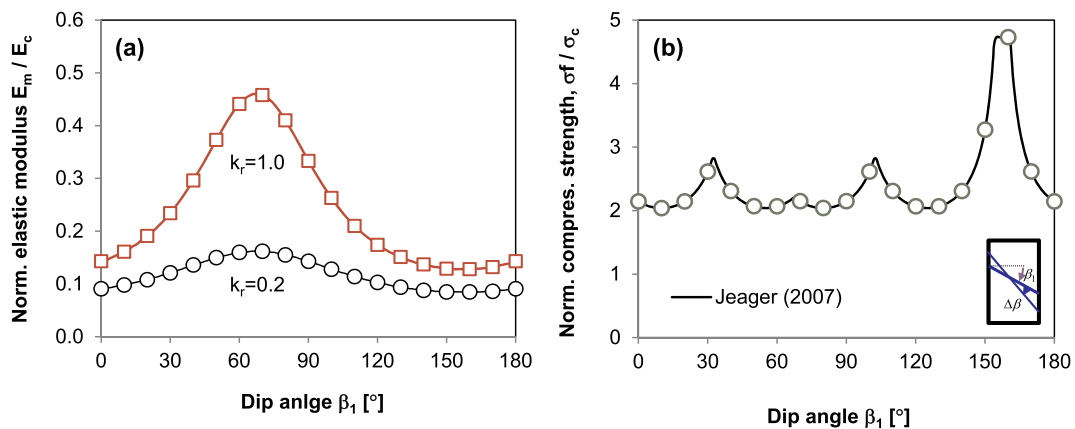


**Figure 3.** Mechanical model validation - Rock mass with two fracture sets subjected to vertical compression. (a) Rock mass stiffness normalized by the intact rock stiffness vs. fracture orientation. (b) Rock mass strength normalized by the confining stress vs. fracture orientation. Confining stress 1.0 MPa. Difference in dip angles  $\Delta = 45^\circ$ . Material parameters in Table 1.

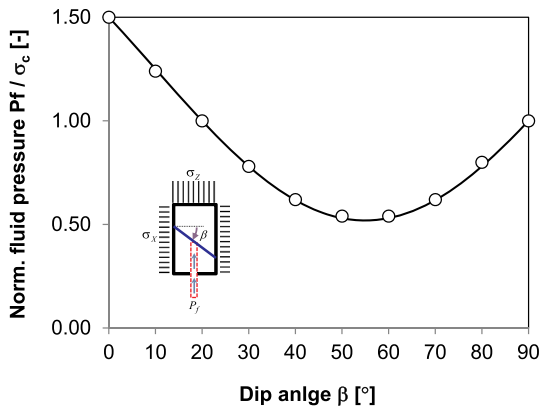


**Figure 4.** Hydro-mechanical coupling - Model validation. Fluid pressure that triggers shear failure. Rock mass with a single fracture set at dip angle  $\beta$ . Lines: analytical solution. Data points: numerical results. Boundary stresses:  $\sigma_x = 1.0\text{MPa}$ ,  $\sigma_z = 1.5\text{MPa}$ . Fracture strength parameters:  $c = 0\text{MPa}$ ,  $\phi = 20^\circ$  (Table 1a)

the bedding plane within intact rock cores.<sup>61</sup>

Hydro-mechanical coupling can induce rock mass failure as the pore pressure increases. We test the numerical simulator against Jaeger's weakness model: the fractured rock mass is subjected to an anisotropic state of stress ( $\sigma_z$ ,  $\sigma_x = \sigma_y$ ) and the fluid pressure gradually increases until the fractured rock mass reaches failure. Analytically, the fluid pressure at failure is

$$P_f = \sigma_x + (\sigma_z - \sigma_x) \frac{\tan(\beta - \phi)}{\tan(\beta - \phi) - \tan(\phi)} \quad (17)$$

where  $\sigma_x$  and  $\sigma_z$  is the horizontal and vertical stresses (sketch in Fig. 4).

Numerically, the fluid injection pressure that triggers shear failure is the last value before numerical instability. Fig. 4 shows the fluid pressure  $P_f$  required to trigger failure as a function of the dip angle  $\beta$ . The analytical solution in Equation (17) matches numerical results (Fig. 4).

#### 4. Example: hydraulic stimulation

The dependency between fluid pressure, effective stress, fracture aperture and fluid flow can lead to complex non-linear effects and instabilities. The implicit joint-continuum model validated above is applied herein to analyze the challenging problem of hydraulic stimulation in fractured rock masses.<sup>62</sup> This is the quintessential example of a hydro-mechanical coupled problem.

Natural fractures are not necessarily oriented normal to the current minimum in-situ stress. Therefore, the in-situ principal stress direction does not necessarily control the direction of maximum flow.<sup>63–65</sup> In fact,

- (i) Small shear displacements can cause significant dilation and a substantial increase in permeability<sup>66,67</sup>; then, fractures aligned with the maximum shear stress will be most conductive in critically stressed fields.
- (ii) The fluid pressure required to reactivate favorably orientated fractures can be lower than  $\sigma_h$ .<sup>68,69</sup>

High-pressure fluid injection may cause<sup>70</sup>: tensile fractures when the fluid pressure exceeds the tensile strength (not explored in this study), opening mode discontinuities along pre-existing fractures (when fluid pressure overcomes the confining stress), or hydro-shearing (Fig. 4).

Let's consider a borehole (diameter of 0.4 m) within a  $40\text{m}_x \times 40\text{m}_y$

analysis domain of unit depth (Fig. 5). The layer is subjected to an initial overburden stress  $\sigma_z = 20\text{MPa}$ , and then kept under vertical plane-strain boundary conditions. The far-field horizontal stresses are  $\sigma_x = 30\text{MPa}$  and  $\sigma_y = 15\text{MPa}$ . For clarity, we simulate a single vertical fracture set and consider three different orientations: perpendicular to the minimum principal stress to favor opening (Set #1:  $\theta = 0^\circ$ ), inclined with respect to the principal horizontal stress directions (Set #2:  $\theta = 30^\circ$ ), and perpendicular to the maximum principal horizontal stress direction to capture an extreme condition of principal stress rotation (Set #3:  $\theta = 90^\circ$ ). Table 1b summarizes the hydro-mechanical properties for the intact rock and the fracture sets (Biot's poroelastic constant is assumed to be  $\alpha = 1.0$ <sup>71</sup>).

**Stage 1: Drilling (at constant fluid pressure).** The borehole is “drilled” in three numerical stages: (1) compute nodal forces caused by the far field effective stresses in the medium without the borehole, (2) remove elements within the borehole and replace them with nodal forces on the borehole wall, (3) gradually relax the forces to zero while the borehole fluid pressure remains equal to the far-field fluid pressure.

The Kirsch solution anticipates a tangential stress concentration around the borehole in a homogeneous continuum. However, the borehole response is intimately related to the orientation of the fracture set, and two concurrent effects take place (Fig. 5a): (1) the increase in the tangential effective stress parallel to the fracture set is taken by the intact rock and causes minor strains, and (2) the radial effective stress release increases the fracture set aperture near the well in the direction normal to the fracture set. Zones of high plastic shear work around the borehole anticipate the development of breakouts (Fig. 5a – See similar results obtained using discrete element simulations in Ref. 72).

**Stage 2: Injection.** After drilling, a constant water flux  $q = 0.02\text{m}^3/(\text{min}\cdot\text{m}_z)$  is applied to the borehole wall. The fracture set controls the response: the fluid pressure increases inside the borehole, propagates into the formation, opens fractures, transmissivity increases and favors fluid flow localization along preexisting fractures (Fig. 5b). Fracture opening and flow localization along preexisting fractures can take place even against the maximum principal horizontal stress, as observed in the contrived case of a single fracture set normal to the major principal horizontal stress (Fig. 5b - Fracture Set #3:  $\theta = 90^\circ$ ). Yet, localization is more pronounced when fractures are co-linear with the minimum principal stress.

In all cases, aperture changes during injection pressurization are quasi-normal to the changes in aperture observed during drilling. The rotation in aperture direction near the wellbore is most prominent in fracture Set #2 ( $\theta = 30^\circ$  - Fig. 5b).

Fracture sets that are co-linear with the principal horizontal stresses develop opening mode discontinuities (Sets #1 and #3). However, the initial shear stress on misaligned fracture sets promotes shear sliding during fluid pressurization (Set #2:  $\theta = 30^\circ$  - See also.<sup>70,73</sup> In this case, the sequence of events during injection-pressurization includes a decrease in normal effective stress on the fracture plane, initial shear sliding, an increase in aperture in response to the diminished normal stress and the shear-induced dilation, invasion of the fluid pressure front along the more transmissive fractures and a further reduction of shear strength.

The fluid pressure increases rapidly inside the borehole. When the injection rate is low, the injection pressure reaches a maximum value when the pressure front interacts with the model boundaries and the flow rate matches the leak-off flux ( $q < 0.02\text{m}^3/(\text{min}\cdot\text{m}_z$  - Fig. 6); in this case, the maximum injection pressure is below the far field normal stress. Higher injection rates produce a transient pressure above the far-field normal stress. The peak injection pressure is smallest for the fracture set that is misaligned to the principal stress directions due to the effective stress dependent hydro-mechanical fracture response: pressurization triggers shear failure at an injection pressure that is lower than the minimum far-field horizontal stress.

**Stage 3: End-of-injection.** The injection pressure decreases when the fluid injection stops, and asymptotically approaches the far field fluid

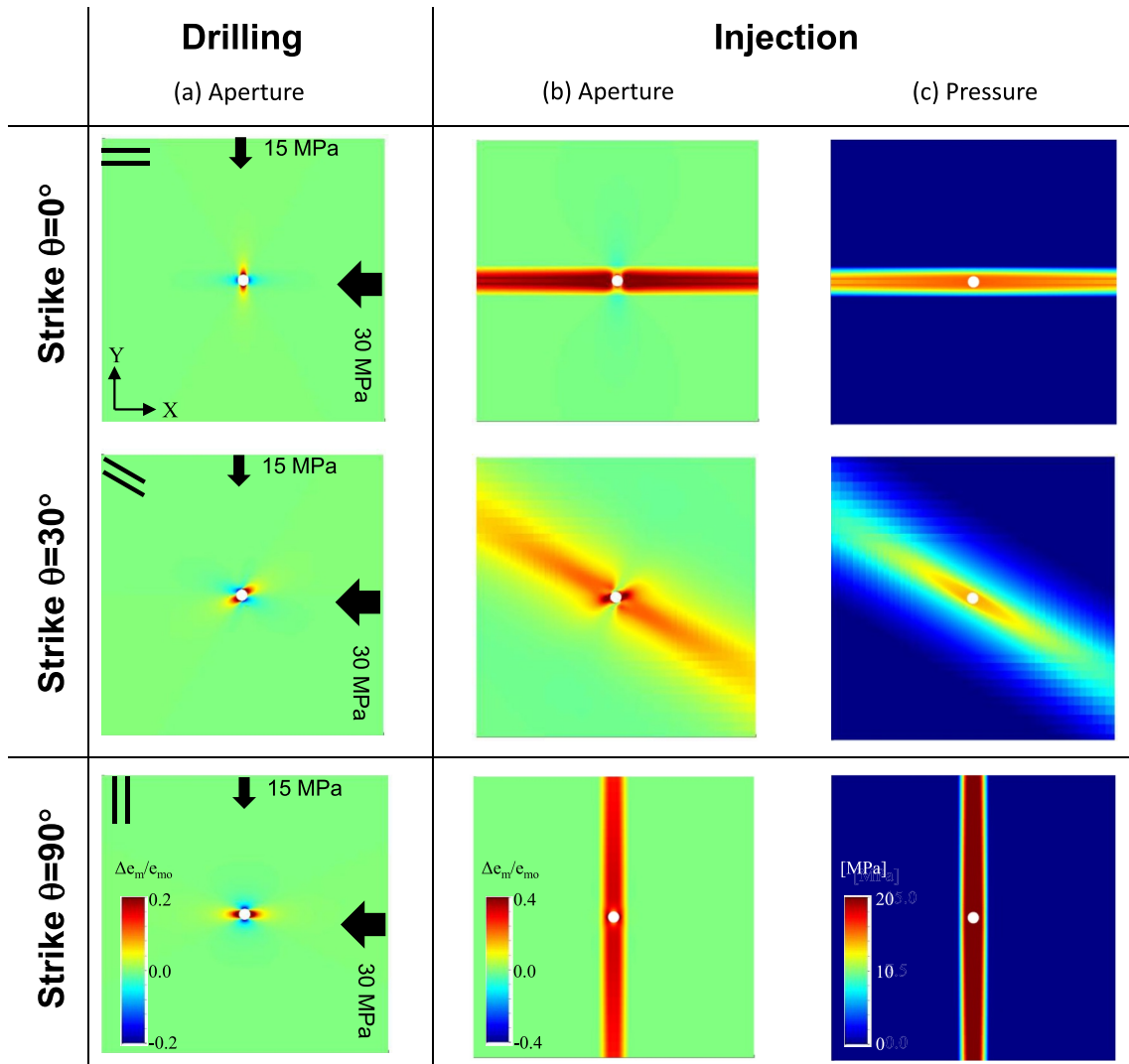


Figure 5. Hydraulic stimulation - Rock mass with a single fractures set. Central borehole in vertical view. (a) Changes in aperture after drilling. (b) Changes in aperture and (c) excess pore pressure during fluid injection. Parameters: Table 1b.

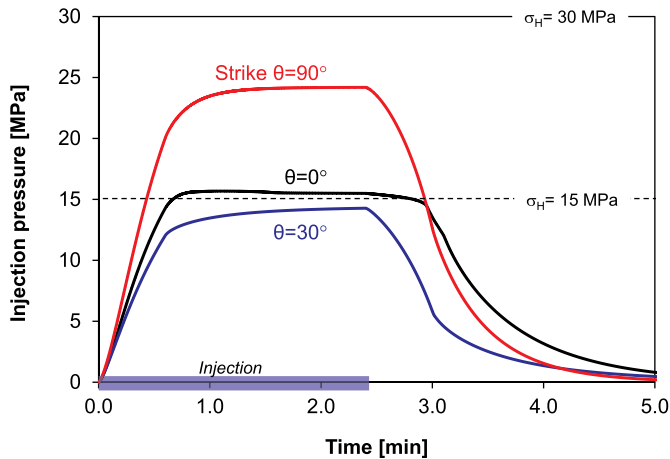


Figure 6. Hydraulic stimulation: Injection pressure vs. time. Rock mass with a single fractures set. Conditions: fluid injection rate  $q = 0.02\text{m}^3/\text{min}/\text{m}$ . Far field stresses  $\sigma_H$  and  $\sigma_h$  shown for reference. Parameters: Table 1b.

pressure, i.e., zero excess fluid pressure. The residual aperture changes are minimal because the currently implemented fracture model does not capture hysteretic aperture behavior.

### 5. Conclusions

Hydro-mechanical coupled processes are common in a wide range of field conditions that involve rock masses. Fractures in the rock mass play a decisive role on the hydraulic and mechanical properties of the rock mass. However, inherent numerical (as well as experimental) challenges hinder comprehensive analyses in most cases.

The choice of numerical model must take into consideration the engineering length scale of interest relative to the fracture spacing. The implicit joint-continuum model developed in this manuscript is applicable for fracture separations that are significantly smaller than the problem size. Hierarchical fracture systems can be modeled as a combination of explicit large fractures embedded in an implicit joint-continuum that represents the rock matrix. The implicit joint-continuum framework facilitates model extensions to study coupled thermo-hydro-chemo-mechanical phenomena in fractured rock masses.

The stiffness and permeability tensors combine the effects of fractures and the intact rock as a linear summation of compliances and the additive contribution of fluid transport, respectively. The effective stress based formulation couples the hydraulic and the mechanical responses within a finite element formulation. The numerical implementation of the coupled hydro-mechanical model is validated against analytical solutions obtained for single and two-fracture sets

under tractable boundary conditions.

Numerical results highlight the prevalent role of fracture sets and their orientation on the evolution of the rock mass during drilling and hydraulic stimulation. In a fractured rock mass, hydraulic fracturing is the opening of preferentially oriented fracture sets. Fractures that are misaligned with the principal stress directions will favor hydro-shearing. Positive hydro-mechanical feedback between aperture, transmissivity, fluid pressure and effective stress can result in fluid flow localization.

## Acknowledgements

This work was supported by the Research Fund (2013-0100) of University of Ulsan.

## Appendix A. Supplementary data

Supplementary data to this article can be found online at <https://doi.org/10.1016/j.ijrmmms.2019.04.006>.

## References

- Goodman RE. *Introduction to Rock Mechanics*. New York: Wiley; 1989.
- Jaeger JC, Cook NGW, Zimmerman RW. *Fundamentals of Rock Mechanics*. fourth ed. Oxford, U.K.: Blackwell; 2007.
- Wasantha PLP, Ranjith PG, Viete DR. Effect of joint orientation on the hydro-mechanical behavior of singly jointed sandstone experiencing undrained loading. *J Geophys. Res. Solid Earth*. 2014;119(3):1701–1717.
- Taron J, Elsworth D, Min KB. Numerical simulation of thermal-hydrologic-mechanical-chemical processes in deformable fractured porous media. *Int. J. R. Mech.* 2009;46:855–864.
- Rutqvist J, Stephansson O. The role of hydromechanical coupling in fractured rock engineering. *Hydrogeol J*. 2003;11:7–40.
- Ellsworth WL. Injection-induced earthquakes. *Science*. 2013;341:142.
- Cundall PA. *UDEC-a generalized distinct element program for modelling jointed rock*. Report PCAR-1-80 US Army Corps of Engineers; 1980.
- Shi G. *Discontinuous Deformation Analysis-A New Numerical Model for the Statics, Dynamics of Block Systems*. Berkeley, USA: PhD thesis. University of California; 1988.
- Gutierrez M, Youn DJ. Effects of fracture distribution and length scale on the equivalent continuum elastic compliance of fractured rock masses. *Journal of Rock Mechanics and Geotechnical Engineering*. 2015;7:626–637.
- Jing L. A review of techniques, advances and outstanding issues in numerical modelling for rock mechanics and rock engineering. *Int. J. Rock Mech. Min. Sci. Geomech.* 2003;40:283–353.
- Sitharam TG, Sridevi J, Shimizu N. Practical equivalent continuum characterization of jointed rock masses. *Int J Rock Mech Min Sci*. 2001;38:437–448.
- Goodman RE, Taylor RL, Brekke TL. A model for the mechanics of jointed rock. *J Soil Mech. Div. ASCE*. 1968;94(SM3):637–659.
- Desai CS, Zamman MM, Lightner JG, Siriwardane HJ. Thin layer element for interfaces and joints. *Int J Numer Anal Methods Geomech*. 1984;8:19–43.
- Agharazi A, Martin CD, Tannant DD. A three dimensional equivalent continuum constitutive model for jointed rock masses containing up to three random joint sets. *Geomech. Geoen. An Int. J.* 2012;7(4):227–238.
- Amadei B, Goodman RE. A 3-D constitutive relation for fractured rock masses. *Proceedings of the International Symposium on Mechanical Behaviour of Structured Media*. 1981; 1981:249–268.
- Bagheri MA, Settari A. Effects of fractures on reservoir deformation and flow modeling. *Can Geotech J*. 2006;43:574–586.
- Huang TH, Chang CS, Yang ZY. Elastic moduli for fractured rock mass. *Rock Mech Rock Eng*. 1995;28(3):135–144.
- Wang TT, Huang TH. A constitutive model for the deformation of a rock mass containing sets of ubiquitous joints. *Int J Rock Mech Min Sci*. 2009;46(3):521–530.
- Yoshida H, Horii H. Micromechanics-based continuum model for a jointed rock mass and excavation analysis of a large scale cavern. *Int J Rock Mech Min Sci*. 2004;41:119–145.
- Bobet A, Fakhimi A, Johnson S, Morris J, Tonon F, Yeung MR. Numerical models in discontinuous media, Review of advances for rock mechanics applications. *J Geotech Geoenviron Eng*. 2009;135(11):1547–1561.
- Oda M. An equivalent continuum model for coupled stress and fluid flow analysis in jointed rock masses. *Water Resour Res*. 1986;22(13):1845–1856.
- Neto EA, de Souza PD, Owen DRJ. *Computational Methods for Plasticity: Theory and Applications*. Wiley; 2008.
- Barton N, Choubey V. The shear strength of rock joints in theory and practice. *Rock Mech*. 1977;10(1-2):1–54.
- Goodman RE. *Methods of Geological Engineering in Discontinuous Rocks*. San Francisco, CA: West Publishing Company; 1976.
- Nguyen TS, Selvadurai APS. A model for coupled mechanical and hydraulic behaviour of a rock joint. *Int J Numer Anal Methods Geomech*. 1998;22:29–48.
- Bandis SC, Lunsden AC, Barton NR. Fundamentals of rock joint deformation. *Int J Rock Mech Min Sci Geomech Abstr*. 1983;20(6):249–268.
- Hobday C, Worthington MH. Field measurements of normal and shear fracture compliance. *Geophys Prospect*. 2012;60:488–499.
- Lubbe R, Sothcott J, Worthington M, McCann C. Laboratory estimates of normal and shear fracture compliance. *Geophys Prospect*. 2008;56:239–247.
- Yoshinaka R, Yamabe T. Joint stiffness and the deformation behavior of discontinuous rock. *Int. J. Min. Sci. Geomech. Abstr*. 1986;23:19–28.
- Plesha ME. Constitutive models for rock fractures with dilatancy and surface degradation. *Int J Numer Anal Methods Geomech*. 1987;11(4):345–362.
- Lee HS, Park YJ, Cho TF, You KH. Influence of asperity degradation on the mechanical behavior of rough rock joint under cyclic shear loading. *Int J Rock Mech Min Sci*. 2001;38:967–980.
- Simo JC, Taylor RL. Consistent tangent operators for rate-independent elastoplasticity. *Comput Methods Appl Mech Eng*. 1985;48:101–118.
- Press WH, Flannery BP, Teukolsky SA, Vetterling WT. *Numerical Recipes in Fortran 77: The Art of Scientific Computing*. Cambridge University Press; 1992.
- Hakami E, Larsson E. Aperture measurements and flow experiments on a single natural fracture. *Int J Rock Mech Min Sci*. 1996;33:395–404.
- Liu E. Effects of fracture aperture and roughness on hydraulic and mechanical properties of rocks: implication of seismic characterization of fractured reservoirs. *J Geophys Eng*. 2005;2(1):38–47.
- Pyrak-Nolte LJ, Nolte DD, Myer LR, Cook NGW, Barton N, Stephansson O, eds. *Fluid Flow through Single Fractures*. Netherlands:Rotterdam: Rock joints; 1990:405–412.
- Barton N, Bandis S, Bakhtar K. Strength, deformation and conductivity coupling of rock joints. *Int J Rock Mech Min Sci Geomech Abstr*. 1985;22:231–245.
- Lee HS, Cho TF. Hydraulic characteristics of rough fractures in linear flow under normal and shear load. *Rock Mech Rock Eng*. 2002;35(4):299–318.
- Souley M, Lopez P, Boulon M, Thoraval A. Experimental hydromechanical characterization and numerical modelling of a fractured and porous sandstone. *Rock Mech Rock Eng*. 2015;48(3):1143–1161.
- Makurat A, Barton N, Rad NS, Bandis S. Joint conductivity variation due to normal and shear deformation. In: Barton N, Stephansson O, eds. *Proceedings International Symposium on Rock Joints, Loen, Norway*. The Netherlands: Rotterdam: Balkema; 1990:535–540.
- Massart TJ, Selvadurai APS. Stress-induced permeability evolution in quasi-brittle geomaterials. *Journal of Geophysical Research (Solid Earth)*. 2012;117. <https://doi.org/10.1029/2012JB009251>.
- Min KB, Rutqvist J, Tsang CF, Jing L. Stress-dependent permeability of fractured rock masses: a numerical study. *Int J Rock Mech Min Sci*. 2004;41:1191–1210.
- Zhang J, Standifird WB, Roegiers JC, Zhang Y. Stress-dependent fluid flow and permeability in fractured media: from lab experiments to engineering applications. *Rock Mech Rock Eng*. 2007;40:3–21.
- Zoback MD, Byerlee JD. The effect of microcrack dilatancy on the permeability of Westerly granite. *J Geophys Res*. 1975;80:752–755.
- Barton CA, Zoback MD, Moos D. Fluid flow along potentially active faults in crystalline rock. *Geology*. 1995;23:683–686.
- Moos D, Barton CA. *Modeling Uncertainty in the Permeability of Stress-Sensitive Fractures*. 42nd US Rock Mechanics Symposium. 2008; 2008 ARMA 08-312.
- Olsson R, Barton N. An improved model for hydromechanical coupling during shearing of rock joints. *Int J Rock Mech Min Sci*. 2001;38(3):317–329.
- Xie N, Jin B, Yang JB, Shao JF. Study on the hydromechanical behavior of single fracture under normal stresses. *KSCE J Civ Eng*. 2014;18(6):1641–1649.
- Witherspoon PA, Amick CH, Gale JE, Iwai K. Observations of a potential size effect in experimental determination of the hydraulic properties of fractures. *Water Resour Res*. 1979;15:1142–1146.
- Kim JM. Hydraulic conductivity and mechanical stiffness tensors for variably saturated true anisotropic intact rock matrices, joints, joint sets, and jointed rock masses. *Geosci J*. 2007;11:387–396.
- Panda BB, Kulatilake PHSW. Effect of joint geometry and transmissivity on jointed rock hydraulics. *J. Engrg. Mech., ASCE*. 1999;125(1):41–50.
- Jing L, Stephansson O. *Fundamentals of Discrete Element Methods for Rock Engineering: Theory and Applications (Developments in Geotechnical Engineering)*. Amsterdam, Netherlands: Elsevier Science; 2007.
- Segura J, Carol I. Coupled HM analysis using zero-thickness interface elements with double nodes. Part I: theoretical model. *Int J Numer Anal Methods Geomech*. 2008;32(18):2083–2101.
- Jiang T, Shao JF, Xu WY, Zhou CB. Experimental investigation and micromechanical analysis of damage and permeability variation in brittle rocks. *Int J Rock Mech Min Sci*. 2010;47(5):703–713.
- Lee SH, Lough MF, Jensen CL. Hierarchical modeling of flow in naturally fractured formations with multiple length scales. *Water Resour Res*. 2001;37:443–455.
- Pinto JL. Deformability of schistose rocks. *Proc., 2nd Congress of the International Society for Rock Mechanics*. vol. I. 1970; 1970:2–30 Beograd, Jugoslavija.
- Cho JW, Kim H, Jeon S, Min KB. Deformation and strength anisotropy of Asan gneiss, Boryeong shale, and Yeoncheon schist. *Int J Rock Mech Min Sci*. 2012;50(12):158–169.
- Duan K, Kwok CY, Pierce M. Discrete element method modeling of inherently anisotropic rocks under uniaxial compression loading. *Int J Numer Anal Methods Geomech*. 2016;40:1150–1183.
- Ramamurthy T, Arora VK. Strength predictions for jointed rocks in confined and unconfined states. *Int J Rock Mech Min Sci Geomech Abstr*. 1994;31:9–22.
- Singh M, Rao KS, Ramamurthy T. Strength and deformational behavior of a jointed rock mass. *Rock Mech Rock Eng*. 2002;35:45–64.
- Yang H, Kim H, Kim K, Min KB. A study of locally changing pore characteristics and hydraulic anisotropy due to bedding of porous sandstone. *Journal of Korean Society For Rock Mechanics*. 2013;23(3):228–240.

62. Economides MJ, Nolte KG. *Reservoir Stimulation*. third ed. John Wiley & Sons; 2000.
63. Heffer K. Geomechanical influences in water injection projects: An overview. *Oil Gas Sci Technol*. 2002;57:415–422.
64. Laubach SE, Olson JE, Gale JFW. Are open fractures necessarily aligned with maximum horizontal stress? *Earth Planet Sci Lett*. 2004;222(1):191–195.
65. Marrett R, Laubach SE, Olson JE. Anisotropy and beyond: Geologic perspectives on geophysical prospecting for natural fractures. *Lead Edge*. 2007;26:1106–1111.
66. Rinaldi AP, Rutqvist J, Sonnenthal EL, Cladouhos TT. Coupled THM modeling of hydroshearing stimulation in tight fractured volcanic rock. *Transport Porous Media*. 2015;108:131–150.
67. Rogers SF. Critical stress-related permeability in fractured rocks. In: Ameen M, ed. *Fracture and In-Situ Stress Characterization of Hydrocarbon Reservoirs*. vol. 209. Geological Society, London: Special Publication; 2003:7–16.
68. Bauer S, Huang K, Chen Q, Ghassemi A, Barrow P. *Laboratory and Numerical Evaluation of EGS Shear Stimulation*. 41st Workshop on Geothermal Reservoir Engineering. Stanford University; 2016 SGP-TR-209.
69. Preisig G, Eberhardt E, Gischig V, et al. Development of connected permeability in massive crystalline rocks through hydraulic fracture propagation and shearing accompanying fluid injection. *Geofluids*. 2015. <https://doi.org/10.1111/gfl.12097>.
70. Gischig V, Preisig G. *Hydro-fracturing versus hydro-shearing: a critical assessment of two distinct reservoir stimulation mechanisms*. 13th International Congress of Rock Mechanics (ISRM 2015). Montreal: Canada; 2015:1–12.
71. Ghassemi A. *Three Dimensional Poroelastic Hydraulic Fracture Simulation Using the Displacement Discontinuity Method*. PhD Thesis. University of Oklahoma; 1996.
72. Duan K, Kwok CY. Evolution of stress-induced borehole breakout in inherently anisotropic rock: insights from discrete element modeling. *J. Geophys. Res. Solid Earth*. 2016;121:2361–2381.
73. Pirayehgar A, Dusseault MB. The stress ratio effect on hydraulic fracturing in the presence of natural fractures. *American Rock Mechanics Association*. Minneapolis, MN, USA. 2014; 2014.